UC San Diego
UC San Diego Previously Published Works

Title

Planar capacitive imaging for composite delamination damage characterization

Permalink

Journal

ISSN

Authors

Gupta, Sumit
Kim, Hyungsuk
Kim, Hyonny
et al.

Publication Date

DOI

Peer reviewed

Planar Capacitive Imaging for Composite Delamination Damage Characterization

Sumit Gupta[1,2], Hyungsuk (Eric) Kim[1], Hyonny Kim[1], and Kenneth J. Loh[1,2,*]

[1] Department of Structural Engineering, University of California San Diego, La Jolla, CA 92093-0085, USA

[2] Active, Responsive, Multifunctional, and Ordered-materials Research (ARMOR) Laboratory, University of California San Diego, La Jolla, CA 92093-0085, USA

[*]Corresponding author, E-mail: kenloh@ucsd.edu

Abstract

The objective of this study is to develop and validate a noncontact, nondestructive inspection and imaging method for rapidly assessing the subsurface condition of carbon fiber-reinforced polymer (CFRP) composite structures. The method works on the principle of planar electrical capacitance tomography (ECT). Unlike conventional ECT systems, electrodes are arranged on a rectangular planar surface in the form of a grid. The volume on one side of the electrode plane is interrogated with an electric field, and the mutual capacitances between the electrodes are measured. The volumetric electrical permittivity distribution of the interrogated region is then reconstructed from the measured capacitance responses. In this work, an ECT image reconstruction algorithm was implemented, and a customized planar capacitive imaging system was prototyped. First, different objects were placed near the electrode array, and the corresponding volumetric change in electrical permittivity was successfully captured. Second, the planar ECT system was employed for detecting artificially introduced subsurface defects in 3D-printed objects. Third, CFRP specimens with different sizes of single-layer delamination were fabricated and subjected to ECT interrogation. The results confirmed that the planar ECT system could detect the location and size of delamination in CFRP panels. The accuracy and resolution of the planar ECT prototype were also characterized.

Keywords: CFRP, composite, delamination, electrical capacitance tomography, nondestructive inspection, planar capacitive imaging, subsurface

1. Introduction

Carbon fiber-reinforced polymer (CFRP) composites are widely used in various aerospace, automotive, and industrial structural components. For example, a high percentage of the fuselage and wings of the Boeing 787 Dreamliner and the Airbus 350 XWB are made of CFRP [1]. The transition from metals to CFRP composites, especially for the aerospace industry, has been motivated by their excellent specific strength and resistance to corrosion [2, 3]. However, CFRP composites can sustain complex damage modes because of their inherent anisotropic characteristics. For example, low-velocity impact can result in subsurface delamination [4]. Delamination cannot be detected by visual inspection and can propagate, resulting in significant reductions in structural strength and stiffness that can jeopardize safety [5]. Therefore, it is crucial to identify such damage in laminated composites so that necessary structural repairs can be conducted in a timely manner.

A plethora of research on structural health monitoring (SHM) and nondestructive inspection (NDI) methods for characterizing damage in CFRP composites has been investigated. Among the various NDI strategies, visual inspection is most predominantly used in practice today but fails to detect subsurface damage. Impact-sensitive coatings and liquid penetrants are often used to enhance its accuracy [6]. On the other hand, damage location and severity in CFRP can be precisely captured by ultrasonic inspection, which are typically operated in the 1 to 50 MHz range [7]. Damage is inferred from time-of-flight and amplitude measurements. Despite the accuracy of ultrasonic NDI methods (*e.g.*, C-scan), the structural component needs to be disassembled from the main structure and immersed in water for ultrasonic scanning. In addition, scanning the entire structural surface is time-consuming. Hence, aircraft operation can be significantly disrupted. Acoustic emission (AE) employs piezoelectric transducers that monitor acoustic waves that are generated by and propagated from growing defects such as cracks [8, 9]. However, AE measurements are highly susceptible to ambient noise, which make damage detection challenging.

A variety of imaging techniques, such as X-ray, has also been employed for characterizing damage in CFRPs [10]. Since carbon fibers have poor X-ray absorptivity, penetrants

(*e.g.*, zinc iodide solution) are used to enhance sensitivity. However, in order for the penetrant to seep through and wet the composite, an initial defect must be created on the composite surface. Thermographic imaging, on the other hand, uses infrared cameras that map the surface temperatures of structures, and changes in the amount of infrared energy radiated can correspond to subsurface structural features or potential damage [11]. Despite their versatility, thermography assumes that the structure has been subjected to uniform heating. Its accuracy also depends on the distance of the damage from the outer surface.

To overcome these aforementioned limitations, another approach is to modify CFRPs with conductive fillers or to embed thin films so that their electrical properties change in response to damage. For instance, Loyola *et al.* [12] embedded piezoresistive carbon nanotube-latex thin films in glass fiber-reinforced polymer composites. An electrical impedance tomography (EIT) measurement strategy and algorithm were implemented for capturing the change in the thin film's distribution of electrical conductivity caused by impact-damage-induced residual strains. Thomas and Tallman [13] also showed that EIT could be used for detecting damage in carbon-black-infused composite specimens of complex shapes and geometries. While these methods could pave the way for new SHM strategies, this approach fundamentally modifies the composite matrix, which may degrade their mechanical performance, and introduces a new challenge of embedding electrodes. More importantly, these new structural composites will require recertification for airworthiness, which is a time-consuming and financially demanding process. Thus, there remains a need to develop sensing techniques that can quickly and accurately identify subsurface damage features.

In this study, a noncontact, portable, NDI system is proposed for imaging and characterization delamination in CFRP composites. The proposed method is based on electrical capacitance tomography (ECT) [14]. In conventional ECT, a circular measurement tool with a set of electrodes interrogates its inner circular region with alternating current (AC) electric fields. The mutual capacitances between electrode pairs are measured, and an inverse problem is solved to reconstruct the electrical permittivity distribution of the region or the cross-section of any object within it. Damage in the object (*e.g.*, cracks or voids) would naturally be of a different permittivity than the pristine structure and could be resolved by ECT permittivity imaging. However, typical CFRP composite panels cannot fit within a circular electrode array and thus cannot be imaged. Therefore, a planar array ECT system, where an array of electrodes is arranged on a rectangular surface, and an ECT algorithm is used to solve for the volumetric electrical permittivity on one side of the electrode plane. The hypothesis is that a planar ECT system can resolve the locations and sizes of delamination (in the form of permittivity changes) in CFRP panels.

This manuscript begins with the mathematical formulation of ECT, followed by the experimental tests and procedures. Next, planar ECT verification and validation test results are presented. Then, the accuracy and resolution of the proposed imaging system were characterized. The manuscript ends with a brief summary of the main findings.

2. ECT Background

The goal of ECT is to reconstruct the electrical permittivity distribution of a predefined sensing region using measured sets of mutual capacitances between pairs of boundary electrodes [14, 15]. In general, electrodes are equidistantly spaced along the interior of a circular apparatus. An electrode is excited with an AC signal to propagate an electric field in the sensing region, and mutual capacitances between the excitation and all other remaining electrodes are measured. This excitation-measurement pattern is repeated for all possible electrode pairs to obtain the full set of mutual capacitance measurements, which is then used as the input to the ECT inverse problem for back-calculating the electrical permittivity distribution.

Since its discovery in the late 1980s, ECT has been successfully used for various industrial process monitoring applications [16-20]. Later, it was also used for NDI of structural components [21-24], as well as for monitoring epoxy curing and subsurface defects in epoxy composites [25, 26]. It was demonstrated that ECT could be coupled with passive thin film sensors to achieve noncontact pH and strain sensing [27, 28]. In all these applications, the imaged target had to be placed inside the circular ECT electrode array. This requirement prohibits the use of conventional ECT for NDI of many structural components, such as structural composites.

In light of these limitations, electrodes can be arranged on a rectangular surface to form a planar ECT system, as depicted in Fig. 1 [29]. While electric field propagation is confined in a 2D plane in conventional ECT systems, it propagates in 3D in the vicinity of the planar electrode array. A grounded metallic shield is employed on the back surface of the electrode array to confine the electric field to one side and to impede external electromagnetic interference (EMI) from corrupting capacitance measurements.

There has been growing interest in using planar capacitive imaging systems for its geometrical advantages. For instance, Wang *et al.* [30] demonstrated the ability of a planar ECT system for surface flow imaging. Planar ECT sensor modeling, its features, and design issues were systematically discussed by Hu and Yang [31]. Their analytical results showed that the planar ECT sensor in single-electrode mode could be employed for material characterization and imaging. In addition, a planar capacitive sensor matrix operating in a single-electrode mode was also proposed by Chen *et al.* [32] for security screening. A mathematical model was derived to determine the design parameters of the sensing system. Diamond *et al.* [33] was able to image various materials (*e.g.*, metals, insulators, fibre-reinforced, polymer composites, and concrete) by using two coplanar electrodes mounted on one surface of the test specimens. Underwater operation of the proposed capacitive imaging system was also successfully
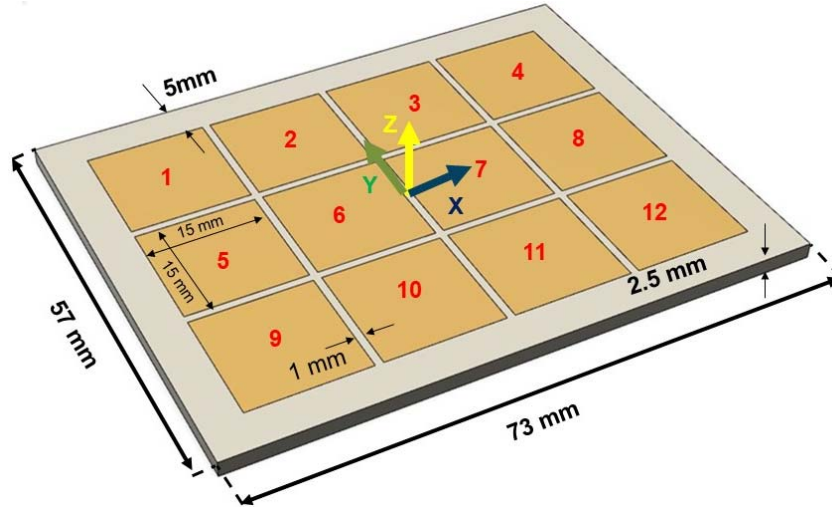
Figure 1. A 12-electrodes planar ECT system was assembled to form a 4×3 rectangular array. The electrode numberings and Cartesian coordinate system used for visualizing the reconstructed images are labeled accordingly.

demonstrated. Ye *et al.* [34] proposed a planar ECT system as a subsurface imaging tool, and system performance was evaluated through rigorous experimental studies. The system successfully detected an object up to a distance of 53% of the length of the electrode array. A three-step automatic parameter selection (APS) algorithm was proposed by Tholin-Chittenden *et al.* [35] for accurately identifying buried objects. This work showed that the effect of regularization, as well as the decrease in sensitivity with increasing distance from the electrode plane, could be addressed by the APS algorithm.

Despite these recent advances in planar ECT systems, the implementation of ECT for imaging CFRP composites is inherently challenging, since the measuring circuit gets shortened due to the presence of the conductive object inside the electrode array [36]. An applied electric field through highly conductive objects forces the inner free charges to move to the surface until the total electric field inside the conductive object is zero. Such charge movement creates an equipotential region on the conductive object, thereby creating a void in the electric field distribution. Despite these challenges, Hosani *et al.* [37] showed that a highly conductive object inside the ECT electrode array could be captured using a high permittivity model as well as by an equal potential model. Li *et al.* [36] also demonstrated that a high-frequency electrical excitation (~2 MHz) could be used to interrogate highly conductive objects for ECT imaging. However, these techniques need to be systematically studied for imaging CFRP composites and when using a planar ECT setup.

Similar to conventional ECT, the planar ECT electrical permittivity reconstruction algorithm consists of the forward and inverse problems. In the forward problem, capacitance responses between pairs of boundary electrodes are estimated, while electrical permittivity distribution in the volume adjacent to the electrode plane is known or assumed. On the

other hand, the inverse problem reconstructs the electrical permittivity distribution from the measured set of mutual capacitances. In previous conventional ECT studies, 2D absolute permittivity reconstruction was achieved by implementing a Gauss-Newton (GN) iterative algorithm [27, 38, 39]. However, the GN algorithm suffers from high computational cost, and it is not suitable for real-time applications. Therefore, in this study, a single-step permittivity reconstruction algorithm was implemented for subsurface damage detection in CFRP composites. The mathematical formulation of the planar ECT forward and inverse problems are described in the next sections.

2.1 ECT forward problem

As mentioned earlier, the ECT forward problem propagates an electric field in the volume adjacent to the electrode plane (Ω), and capacitance response is calculated. Ω is also known as the region of interest considered for the permittivity reconstruction. The electric field distribution (u) in Ω can be mathematically modelled by 3D Laplace's equation as shown in equation 1:

$$\nabla \cdot (\boldsymbol{\varepsilon} \nabla \boldsymbol{u}) = 0 \tag{1}$$

where $\boldsymbol{\varepsilon}$ is the electrical permittivity distribution in Ω. Here, the applied electrical field was modeled as an electrostatic field assuming steady-state conditions (*i.e.*, there was no accumulation of electrical charges inside Ω). This second-order partial differential equation (*i.e.*, equation 1) needs to be solved with proper boundary conditions to evaluate u at every location within Ω, which is accomplished using equation 2:

$$\boldsymbol{u} = V \tag{2}$$

where V is the magnitude of the applied electrical voltage at the excitation electrode. V is set to zero for all the remaining electrodes. Finite element (FE) modeling was implemented to numerically solve equation 1 with the boundary conditions specified in equation 2. The weak form of equation 1 was derived by multiplying it with a sufficiently smooth test function (v) and integrating it over the entire Ω.

$$\int_{\Omega} \boldsymbol{\varepsilon} \nabla \boldsymbol{u} \cdot \nabla \boldsymbol{v} dx^3 = 0 \tag{3}$$

In this study, four-node linear tetrahedral elements were used to discretize Ω. A set of linear equations was derived by implementing the boundary conditions in equation 3. These equations can be expressed in matrix form, as shown in equation 4:

$$\boldsymbol{KU} = \boldsymbol{I} \tag{4}$$

where $\boldsymbol{K}$ is the stiffness matrix of the system, $\boldsymbol{U}$ is the vector containing the electrical potential distribution at each node of the FE mesh, and $\boldsymbol{I}$ is the force vector obtained from the boundary conditions. Once $\boldsymbol{U}$ was evaluated, equation 5 was used to estimate the mutual capacitance ($C_{i,j}$) between the ith and jth electrode.

$$C_{i,j} = \frac{1}{V} \int_{e_j} \boldsymbol{\varepsilon} \frac{\partial u_i}{\partial \boldsymbol{n}} dx^2 \qquad i=1{:}l \; ; j=i+1{:}l \tag{5}$$

where e_j is the area corresponding to the jth electrode, $\boldsymbol{u}_i$ is the solution of the forward problem when the ith electrode is used for excitation, $\boldsymbol{n}$ is the unit inward normal to the electrode plane, and l is the total number of boundary electrodes. The finite difference method was utilized to numerically evaluate equation 5.

2.2 Inverse problem

The purpose of the ECT inverse problem is to reconstruct the electrical permittivity distribution of Ω using experimentally measured capacitance responses. A least-squares approach was used:

$$\arg\min_{\Delta\boldsymbol{\varepsilon}} \|\Delta\boldsymbol{C} - \boldsymbol{J}\Delta\boldsymbol{\varepsilon}\|^2 \tag{6}$$

where $\Delta\boldsymbol{C}$ is the observed change in boundary capacitance distribution between two states, $\boldsymbol{J}$ is the sensitivity matrix, and $\Delta\boldsymbol{\varepsilon}$ is the change in electrical permittivity between two states.

Being ill-posed in nature, the optimization problem defined in equation 6 fails to generate meaningful results. Therefore, the ill-posed tomographic inverse problem was regularized by adding a penalty term to the cost function (equation 6):

$$\Delta\boldsymbol{\varepsilon} = \arg\min \|\Delta\boldsymbol{C} - \boldsymbol{J}\Delta\boldsymbol{\varepsilon}\|^2 + \alpha^2 \|\boldsymbol{R}(\Delta\boldsymbol{\varepsilon} - \Delta\boldsymbol{\varepsilon}_0)\|^2 \tag{7}$$

where $\boldsymbol{R}$, α, and $\Delta\boldsymbol{\varepsilon_0}$ are the regularization matrix, regularization parameter, and some prior assumption about the permittivity change, respectively. The regularized inverse problem was formulated by expanding the right-hand-side of equation 7 into its quadratic form and expressed as a function (f) of $\Delta\boldsymbol{\varepsilon}$.

$$\begin{aligned} \boldsymbol{f}(\Delta\boldsymbol{\varepsilon}) = {} & \Delta\boldsymbol{\varepsilon}^T \boldsymbol{J}^T \boldsymbol{J}\Delta\boldsymbol{\varepsilon} - 2\Delta\boldsymbol{\varepsilon}^T \boldsymbol{J}^T \Delta\boldsymbol{C} + \Delta\boldsymbol{C}^T \Delta\boldsymbol{C} \\ & + \alpha^2 \Delta\boldsymbol{\varepsilon}^T \boldsymbol{R}^T \boldsymbol{R}\Delta\boldsymbol{\varepsilon} - 2\alpha^2 \Delta\boldsymbol{\varepsilon}^T \boldsymbol{R}^T \boldsymbol{R}\Delta\boldsymbol{\varepsilon}_0 \\ & + \alpha^2 \Delta\boldsymbol{\varepsilon}_0^T \boldsymbol{R}^T \boldsymbol{R}\Delta\boldsymbol{\varepsilon}_0 \end{aligned} \tag{8}$$

To optimize equation 8, its derivative was calculated in an arbitrary direction ($\boldsymbol{x}$), as shown in equation 9.

$$\begin{aligned} \boldsymbol{x}^T \nabla \boldsymbol{f}(\Delta\boldsymbol{\varepsilon}) = {} & 2\boldsymbol{x}^T \boldsymbol{J}^T \boldsymbol{J}\Delta\boldsymbol{\varepsilon} - 2\boldsymbol{x}^T \boldsymbol{J}^T \Delta\boldsymbol{C} \\ & + 2\alpha^2 \boldsymbol{x}^T \boldsymbol{R}^T \boldsymbol{R}\Delta\boldsymbol{\varepsilon} - 2\alpha^2 \boldsymbol{x}^T \boldsymbol{R}^T \boldsymbol{R}\Delta\boldsymbol{\varepsilon}_0 \end{aligned} \tag{9}$$

Equation 9 was set to zero to evaluate $\Delta\boldsymbol{\varepsilon}$ for any $\boldsymbol{x}$.

$$\Delta\boldsymbol{\varepsilon} = \left(\boldsymbol{J}^T \boldsymbol{J} + \alpha^2 \boldsymbol{R}^T \boldsymbol{R} \right)^{-1} \left(\boldsymbol{J}^T \Delta\boldsymbol{C} - \alpha^2 \boldsymbol{R}^T \boldsymbol{R}\Delta\boldsymbol{\varepsilon}_0 \right) \tag{10}$$

In general, $\Delta\boldsymbol{\varepsilon_0}$ was set to 0 to obtain the most generalized form of the solution of $\Delta\boldsymbol{\varepsilon}$:

$$\Delta\boldsymbol{\varepsilon} = \left(\boldsymbol{J}^T \boldsymbol{J} + \alpha^2 \boldsymbol{R}^T \boldsymbol{R} \right)^{-1} \boldsymbol{J}^T \Delta\boldsymbol{C} \tag{11}$$

In this study, $\boldsymbol{R^T R}$ and α were assumed to be diag($\boldsymbol{J^T J}$) and 10^{-2}, respectively [40]. Then, the sensitivity method was adopted to compute $\boldsymbol{J}$ [41]:

$$\boldsymbol{J} = \frac{\partial \boldsymbol{C}_{i,j}}{\partial \boldsymbol{\varepsilon}_k} = \frac{\int_{\Delta_k} \nabla \boldsymbol{u}_i \cdot \nabla \boldsymbol{u}_j dx^3}{V} \tag{12}$$

where ε_k and Δ_k are the electrical permittivity and the volume of the kth finite element in Ω, while $\boldsymbol{u}_i$ and $\boldsymbol{u}_j$ are the solutions of the forward problem when the ith and jth electrodes were used for electrical excitation, respectively. $\boldsymbol{J}$ was evaluated for the entire Ω and was used for permittivity reconstruction.

3. Experimental Details

3.1. Planar ECT system

A prototype planar ECT system was designed and assembled in this work. A polylactic acid (PLA) rectangular plate ($73\times57\times2.5$ mm^3) was 3D-printed using an Ultimaker 3+. Here, 12 copper tape boundary electrodes, each 15×15 mm^2, were arranged in a 4×3 pattern on the surface of the PLA plate as shown in Fig. 1. A copper shield was affixed onto the opposite face of the PLA plate to minimize EMI effects. RG 174 cables were used to connect the electrode array to the ECT data acquisition (DAQ) unit. A commercialized high-speed capacitance measuring unit was employed for ECT interrogation and data acquisition, which outputted 1.25 MHz, 15 V peak-to-peak, square waves for interrogation. During data interrogation, only independent measurements (*i.e.*, $12\times11/2=66$ measurements) were acquired and used for solving the ECT inverse problem.
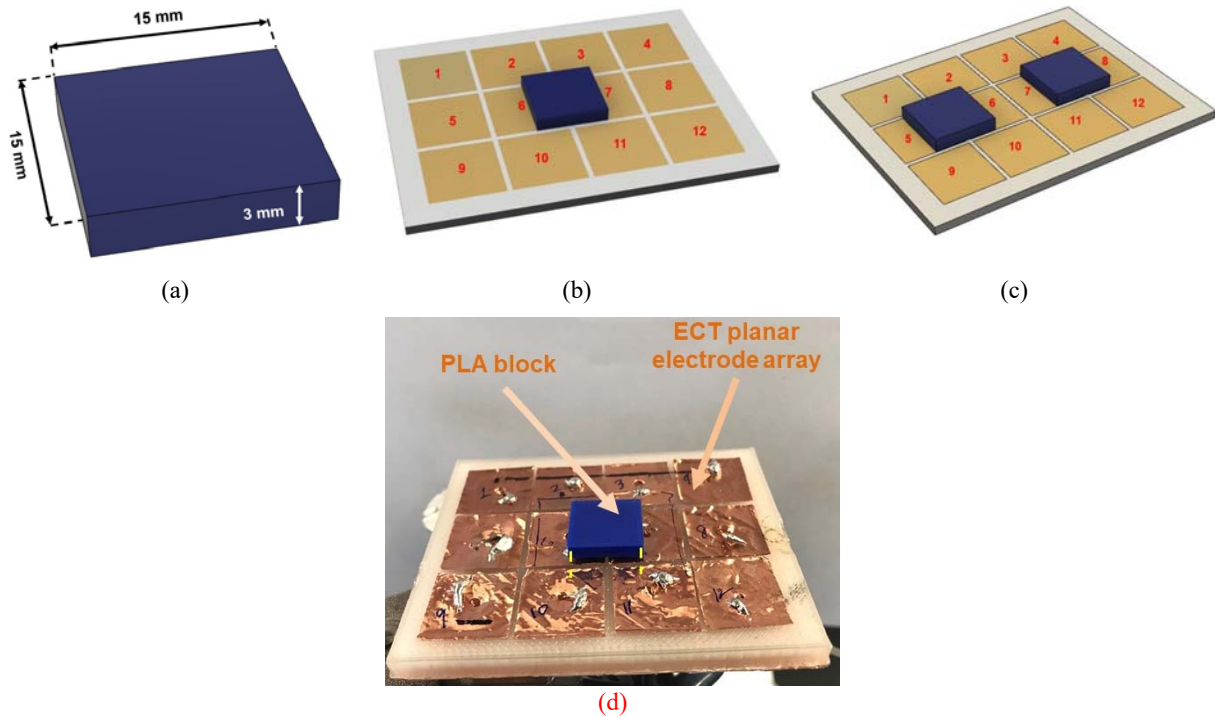
Figure 2. (a) PLA blocks 15×15×3 mm³ in size were 3D-printed for planar ECT validation. (b) A PLA block was placed at the center of the ECT electrode array. (c) Two PLA blocks were simultaneously imaged using the planar ECT system. (d) The experimental test setup is shown.

3.2 Planar ECT validation

The planar ECT system was validated for detecting and imaging the presence of objects in its sensing region. The experiments involved placing 3D-printed 15×15×3 mm³ PLA blocks (Fig. 2a) at different locations in Ω. First, a PLA block was placed at the center of the electrode array (*i.e.*, between electrodes-6 and -7) as shown in Fig. 2b. Second, two PLA blocks were placed along the central row of the electrode array between electrodes-5 and -6, and -7 and -8 (Fig. 2c), and ECT measurements were recorded for permittivity reconstruction. A baseline ECT measurement was also acquired prior to the placement of any objects. Fig. 2d shows a picture of the test setup with a PLA block placed at the center of the electrode array.

3.3 Subsurface damage detection validation

The second set of experiments aimed to detect subsurface damage (that physically resembled composite delamination) in 3D-printed specimens. The Ultimaker 3+ was employed to 3D-print 30×30×6 mm³ PLA specimens with 15×15 mm² internal voids of different thicknesses (*i.e.*, t = 2, 3, and 4 mm). The dimensions of the 3D-printed specimen are illustrated in Fig. 3a. Each specimen was kept at the center of the sensing region as shown in Fig. 3b, while ECT measurements were recorded. In addition, a pristine PLA specimen without a void

was fabricated and was subjected to ECT interrogation by placing it at the same location as the damaged specimen.

3.4 Damage detection in CFRP

Five CFRP panels of sizes 30×30×3 mm³ with $[0]_{10}$ plies and with different sizes of single-layer delamination were fabricated by vacuum-assisted resin transfer molding (VARTM) (Fig. 4). These CFRP panels were fabricated by stacking 10 layers of plain weave carbon fiber fabric (Hexcel 282 plain weave fabric) and infusing them with SC-780 epoxy (Applied Poleramic Inc.). The flow of resin throughout the stacked fabrics was assisted by applying vacuum. Delamination was purposely introduced by lacing rectangular release film (WL5200) of 2×2, 4×4, 6×6, 8×8, and 10×10 mm² in size between the fifth and sixth carbon fiber layers prior to epoxy infusion (*i.e.*, approximately at a depth of ~1.5 mm). These five specimens with ascending damage sizes are referred as D1, D2, D3, D4, and D5 (see Table 1). An additional undamaged CFRP panel was also fabricated to serve as the undamaged baseline. Each CFRP specimen was then placed at six different locations in the sensing region, which is noted as P1, P2, P3, P4, P5, and P6 in Fig. 5, and was subjected to ECT testing. Similar to Section 3.3, the differences in capacitance measurements corresponding to the damaged and undamaged specimens were used for electrical permittivity reconstruction.
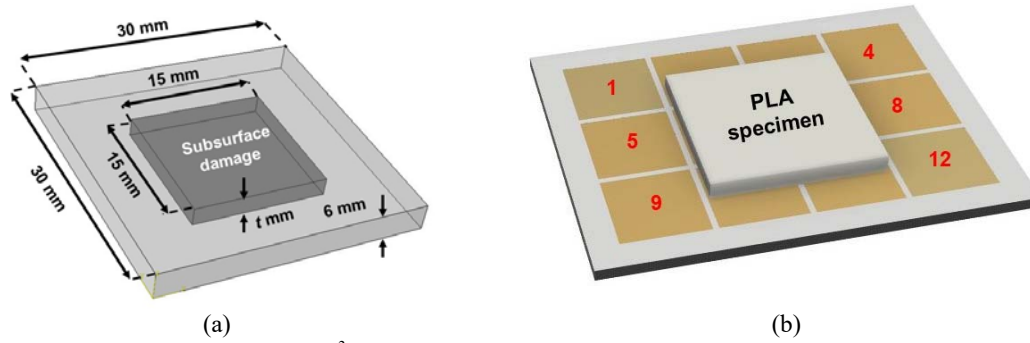
Figure 3. (a) PLA panels 30×30×6 mm³ in size were 3D-printed with internal rectangular voids of different thicknesses.
(b) The "damaged" PLA specimens were placed at the center of the electrode array and subjected to ECT interrogation.

4. Results and Discussion

4.1 Foreign object detection

Section 3.2 described the volumetric permittivity imaging tests, where PLA blocks were placed at different positions on the ECT electrode array. ECT volumetric permittivity results (with respect to the empty baseline) were obtained. To better visualize these results, 2D planar sections were considered with respect to the *x*, *y*, and *z* axes as defined in Fig. 1 and illustrated in Fig. 6. The *z*-plane was defined to slice through the middle of the PLA specimens (*i.e.*, at a height of 1.5 mm from the electrode array). First, the ECT test results for the case of a single PLA block are shown in Fig. 7, where the changes in permittivity distribution with respect to the empty baseline are shown for all three *x*, *y*, and *z* planar sections. An increase in electrical permittivity was observed at the center of the sensing region where the PLA specimen was located.

This permittivity increase is expected since PLA is of a higher electrical permittivity than air. Second, two identical PLA blocks were placed in a row (Fig. 2c) and subjected to ECT interrogation, and the *z*- and *y*-plane results are shown in Fig. 8. Only these two sections were considered since the *x*-plane sectional cut did not intersect the PLA blocks.

For both test cases, electrical permittivity distributions in the *z*-plane correctly and accurately located the positions of the PLA blocks. The electrical permittivity distributions in the *y*- and *x*-planes show the cross-section of the PLA blocks. However, it can be seen from Figs. 7b, 7c, and 8b that the dimensions of the PLA specimens were slightly exaggerated near the base while gradually decreasing with increasing distance from the electrode plane. This nonuniformity was observed due to the higher sensitivity of the planar ECT system near the electrode plane, where denser electric field lines are expected. Although ECT did not accurately reconstruct the PLA blocks' cross-sectional shapes, their size and locations were successfully characterized.

4.2 Subsurface damage detection

After successfully validating the planar ECT system in section 4.1, the next set of experiments investigated the ability

of ECT to image subsurface damage in PLA specimens. The same *x*-, *y*-, and *z*-planes were used for visualizing the ECT results, with the exception that the *z*-plane sliced through the middle of the 6-mm-thick PLA specimen (*i.e.*, at 3 mm).

The ECT results in Fig. 9 show the difference in electrical permittivity distributions between the damaged and undamaged specimens. The changes in permittivity are shown to better visualize delamination as detected by ECT. First, for all the results shown in Fig. 9, the position of damage was correctly identified to be in the center of the sensing region. Second, a decrease in electrical permittivity was observed. This result is expected, since these internal damage features are equivalent to a thin air void, and air has a lower permittivity than PLA. Last, it was found that the magnitude of permittivity changes increased with increasing damage thickness. Again, these results make sense since thicker delamination features contained more air than smaller ones.

However, the estimated damage sizes were slightly larger than the actual cases. The overestimations could have resulted from the limited number of measurements that were used for image reconstruction (*i.e.*, using a 12-electrode system). More boundary electrodes would result in additional independent capacitance measurements and would enhance the accuracy and resolution of the reconstructed images. Also, it is well known that L2 regularization, which was used in this study, reduces the sharpness of reconstructed images. Future work can consider using higher excitations voltages along with an L1 regularization scheme (*e.g.*, total variation regularization) to enhance image quality. Nevertheless, the results presented in Figs. 8 and 9 successfully validated that the proposed planar ECT system could characterize the location and severity of subsurface defects in 3D-printed specimens.

4.3 ECT imaging of CFRP delamination

The objective of the final tests described in section 3.4 was to validate using a planar ECT system for imaging delamination in CFRP panels. Five CFRP panels with various single-layer delamination sizes were fabricated. Ultrasonic C-scan using a 10 MHz focused transducer confirmed the sizes and locations of the embedded damage features (Fig. 10). It
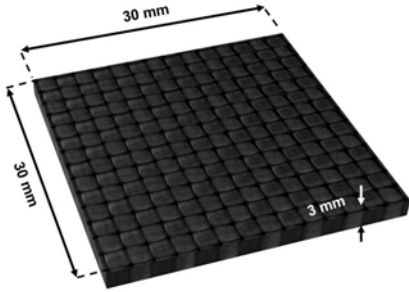
Figure 4. CFRP panels with different sizes of single-layer delamination were fabricated by VARTM .

Table 1. Sizes of delamination in CFRP panels

Damage case	Damage size [mm²]
D1	2×2
D2	4×4
D3	6×6
D4	8×8
D5	10×10

(a)	(b)	(c)
(d)	(e)	(f)
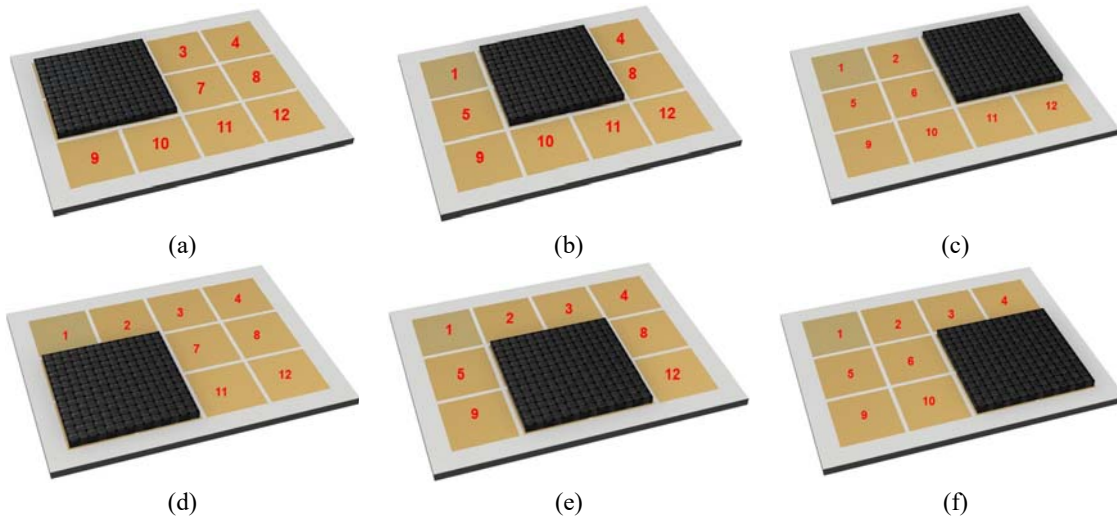
Figure 5. Pristine and damaged CFRP specimens were subjected to ECT interrogation by placing them at the (a) top-left, (b) top-middle, (c) top-right, (d) bottom-left, (e) bottom-middle, and (f) bottom-right region on the electrode array. These six positions are designiated as P1, P2, P3, P4, P5, and P6, respectively.

should be mentioned that "thickness" in the color bar of Fig. 10 was estimated from the measured time-of-flight of the applied ultrasound excitation. This thickness indicates the depth from where the ultrasonic signal was reflected. Note that delamination was introduced between the fifth and sixth ply (*i.e.*, at a depth of ~1.5 mm), while the entire CFRP panel was ~3 mm thick. Although delamination was confirmed in cases D2 to D5, no damage was identified by C-Scan for the D1 case (Fig. 10a).

These panels were then placed at six different positions on top of the electrode array for ECT testing, and the change in electrical permittivity distributions between the damaged and pristine specimens were determined. Fig. 11 summarizes all the results obtained (*i.e.*, ECT permittivity maps in the *z*-plane at $z = 1.5$ mm). For all the D2 to D5 cases and all positions, a localized decrease in permittivity was observed. It can be observed that variations in damage positions were prominent in the reconstructed images (*e.g.*, at P1, for damage cases D2 to D5), which could be due to slight position mismatches when

placing different CFRP panels on the electrode array for ECT scanning. Inconsistency in damage positions could also be due to variations in the void content from specimen to specimen.

In addition, it was found that image quality significantly deteriorated when CFRP panels were placed at the corners (*e.g.*, at P3 and P6). It is possible that electrodes at the corners were not accurately placed during fabrication or was slightly pulled out of alignment during soldering. As a result, the quality of the reconstructed image at P3 and P6 were not satisfactory. Although it could be difficult to accurately locate damage position in these images, the presence and severity of damage could be easily identified from the decrease in electrical permittivity.

To better quantify these ECT results, the maximum change in electrical permittivity for each damage state and position combination is plotted as a function of its position on the electrode array in Fig. 12. Fig. 12 shows that the magnitudes of maximum permittivity change were consistent for each damage state and did not vary with respect to their positions.
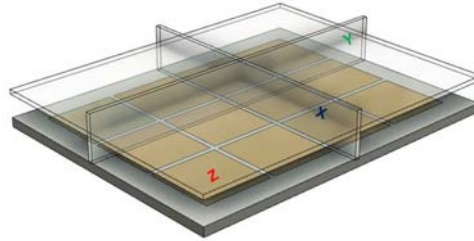
Figure 6. ECT results were visualized by considering *x*-, *y*-, and *z*-planar sections.
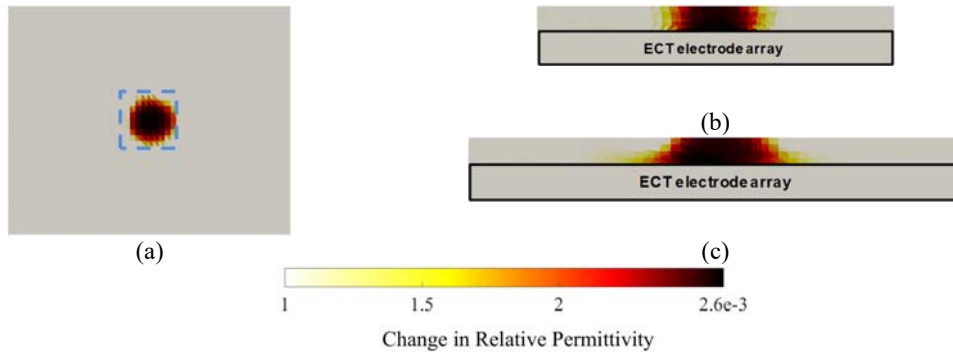

Figure 7. ECT results corresponding to the test where a PLA block was placed at the center of the electrode array were obtained. The permittivity distributions for (a) *z*-, (b) *x*-, and (c) *y*-planes are plotted to show the change in permittivity distribution due to the presence of the PLA block.
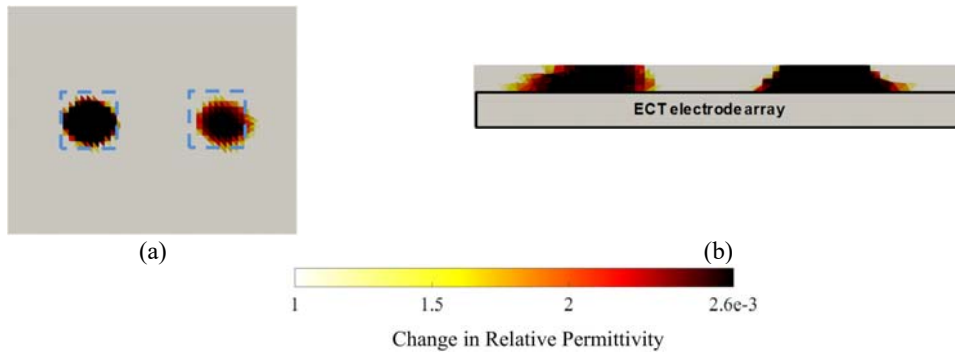

Figure 8. Two identical PLA blocks were placed on the electrode array. The (a) *z*- and (b) *y*-planar sections of the ECT results clearly show the sizes and locations of the PLA blocks.

This result confirmed the robustness of the image reconstruction algorithm. In addition, Figs. 11 and 12 also confirmed that the magnitude of maximum change in permittivity increased in tandem with increasing delamination size.

The depth of the delamination plane could also be identified from the *x*- and *y*-planar views of the reconstructed permittivity maps. However, the interrogating electric field decays quickly with increasing distance from the electrode plane, which affects detectability of permittivity changes. Future studies will be conducted to explore how far the electric field can propagate from the electrode plane in order to obtain an accurate image. Overall, these results successfully validated the proposed planar ECT system for noncontact subsurface delamination characterization in CFRP panels.

4.4. Position accuracy analysis

The accuracy of planar ECT in identifying the location of delamination damage in CFRP panels was critically assessed by computing each ECT image's position error (*PE*). *PE* was calculated as discussed in Adler *et al*. [42]. In short, ECT images were converted to binary (black and white) images to isolate relevant features. The image conversion threshold was set to one-sixth of the average permittivity, which is referred to as the one-sixth amplitude set or $[\varepsilon_q]_i$). More specifically, $[\varepsilon_q]_i$ contains all the image pixels ($[\varepsilon]_i$) greater than one-sixth of the average amplitude of all the image pixels. This threshold was set to exclude noise and other image artifacts while sufficiently characterizing relevant image features for analysis. Mathematically, this can be described as:
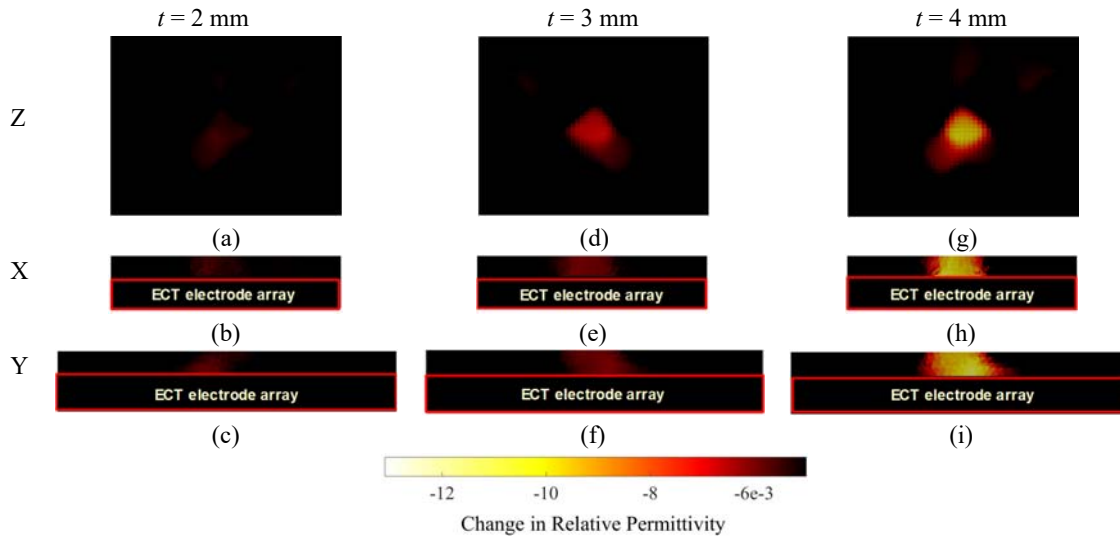
Figure 9. ECT tests were performed on PLA panels with an embedded void that was 2, 3, and 4 mm in thickness. The change in electrical permittivity distributions (with respect to the undamaged baseline) for each damage case and in the (a) to (c) *z*-, (d) to (f) *x*-, and (g) to (i) *y*-planar sections are shown.

$$[\varepsilon_q]_i = \begin{cases} 1 \text{ if } [\varepsilon]_i \geq \frac{1}{6} \max[\varepsilon] \\ 0 \text{ otherwise} \end{cases} \qquad (13)$$

where $[\varepsilon]$ is the reconstructed permittivity distributions shown in Fig. 11.

The procedure began with importing the reconstructed permittivity map (Fig. 11) and converting it grayscale before evaluating $[\varepsilon_q]_i$. The center-of-gravity (CG) of $[\varepsilon_q]_i$ (r_t) was calculated with respect to the top-left corner of the highlighted regions in the images shown in Fig. 11 (*i.e.*, the white dotted boxes) using a Cartesian coordinate system:

$$r_t = \sqrt{\frac{\sum_{i=1}^{n} x_i}{n}} \qquad (14)$$

where x_i is the distance of the ith element in the one-sixth amplitude set from the top-left corner of the image region, and n is the number of voxels in the one-sixth amplitude set. Similarly, C-scan images (Fig. 10) were also processed using a binary image filter:

$$[\sigma_q]_i = \begin{cases} 1 \text{ if } [\sigma]_i \geq 127.5 \\ 0 \text{ otherwise} \end{cases} \qquad (15)$$

where ($[\sigma_q]_i$) contains all the image pixels greater than 127.5 (*i.e.*, half of the entire grayscale limit), and $[\sigma]_i$ is the set of all the image pixels. This process separated the delamination region from other image artifacts. The CG of the largest and isolated delamination region (r_q) was then evaluated with respect to the same coordinate system as the ECT results. The last step was to evaluate *PE*, which is the relative position difference between the ECT and C-scan images:
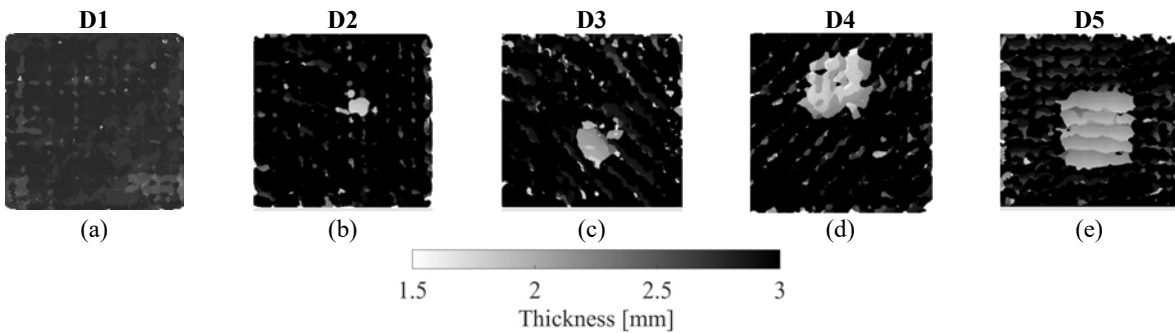

Figure 10. C-scan images of (a) D1, (b) D2, (c) D3, (d) D4, and (e) D5 cases show the exact location of delamination embedded in the CFRP panels.
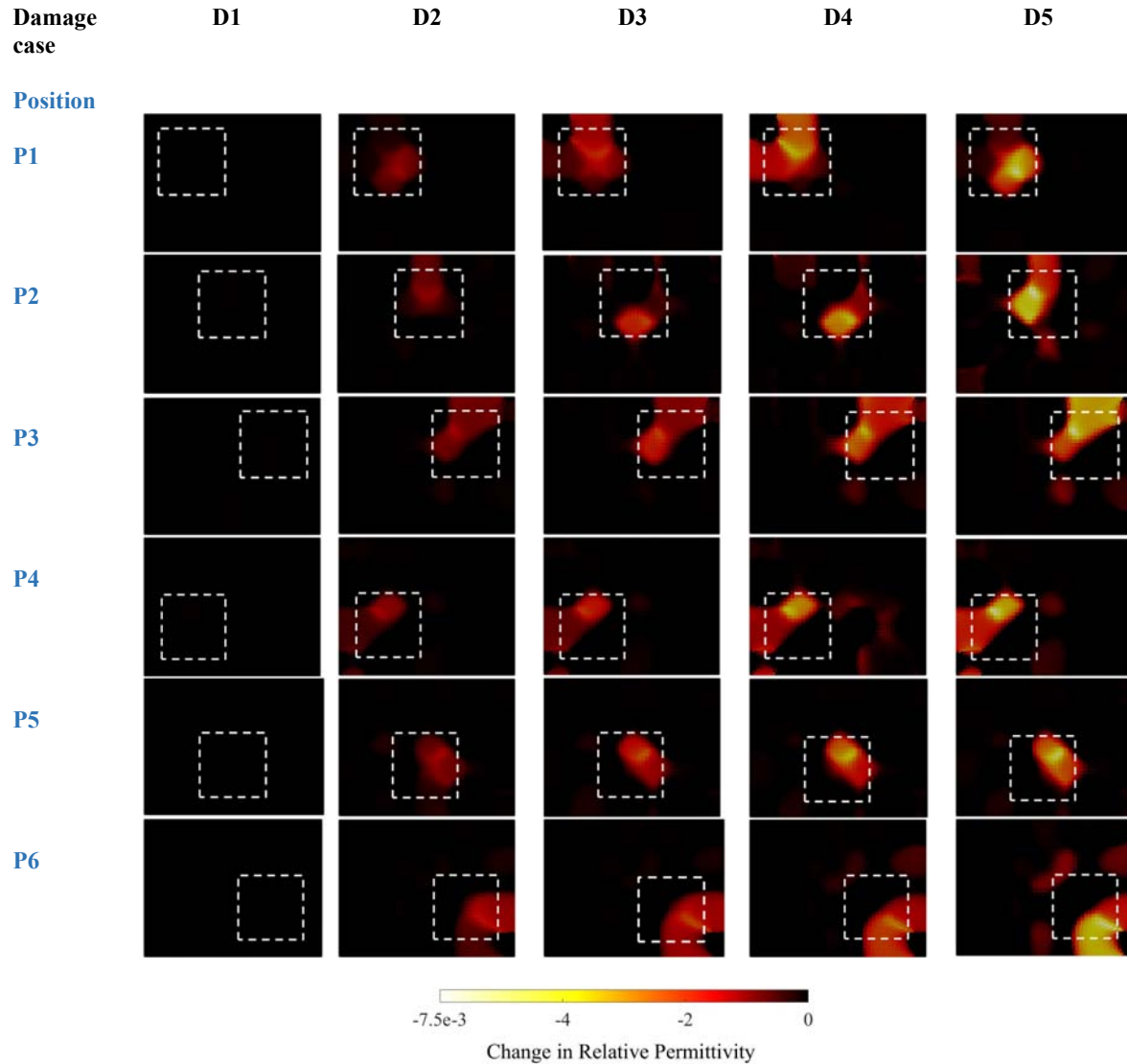
9

Figure 11. CFRP panels with single-layer delamination (D1 to D6) were placed at different positions on the electrode array (P1 to P5) and imaged using the planar ECT system. The change in permittivity distribution (with respect to its corresponding undamaged baseline) was reconstructed, and the ECT permittivity map in the *z*-plane are shown. The exact locations of the CFRP panels are highlighted by the white dotted boxes.

$$PE = |r_t - r_q| \qquad (16)$$

PE corresponding to different damage cases and positions are listed in Table 2. Since D1 was neither detected by C-scan nor by planar ECT, *PE* was not evaluated for this case. For all others, *PE* varies from 2.73 mm to 13.44 mm, and the largest values of *PE* were observed when the specimen was placed at P6. Overall, Table 2 shows that *PE* varied seemingly randomly, which could be due to the nonuniform sensitivity of the planar ECT system. The void contents and their distributions could have influenced the electric field propagation, thereby resulting in larger *PE* in the

reconstructed ECT images. These errors could also be due to the fact that the planar ECT electrode array was fabricated by hand. Slight variations in electrode sizes and positions could contribute to larger position errors. Future work will consider machining and copper etching for fabricating electrode arrays with tighter geometrical tolerances.

4.5 Resolution analysis

In addition to position error, the resolution or smallest damage feature that could be reliably detected by the planar ECT system was also quantified. It was hypothesized that an
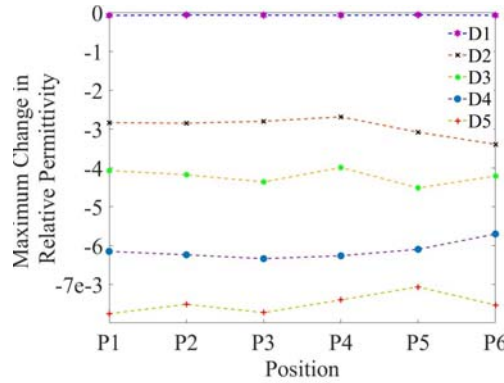
Figure 12. The maximum change in electrical permittivity corresponding to different damage cases were plotted as a function of the different positions.

Table 2. Planar ECT imaging position error results

Position	Damage cases	Position error [mm]			
		D1	D2	D3	D4	D5
P1		-	4.96	5.97	3.64	3.06
P2		-	7.24	5.26	5.39	8.34
P3		-	5.23	3.76	3.54	8.17
P4		-	7.68	5.30	5.31	8.28
P5		-	2.73	5.46	5.06	6.89
P6		-	7.91	9.38	13.44	7.44

image could only be reconstructed if the power of the recorded measurements (*i.e.*, the difference between the measurements corresponding to the damaged and undamaged states) was higher than the power of noise in the measured set of capacitance responses.

First, to quantify the power of the measurement noises, the undamaged CFRP panel was placed at each position. ECT measurements were recorded twice. The differences between the two measurement sets corresponded to noise and were recorded. The root mean square (RMS) values were calculated to estimate noise power, and the square of the RMS values for each position are summarized in Table 3.

Second, the square of the RMS values of the difference in the signals between the undamaged and damaged specimens were estimated through FE simulations. FE simulation was adopted to precisely determine the signal strength, which can be difficult to evaluate by experiments since noise and slight position mismatches could significantly affect the results. The finite element model was implemented to match the experimental conditions used in this study. The simulation began with the initial assumption that the entire sensing region

was filled with air ($\varepsilon = 1$). The relative permittivity of CFRP panels (*i.e.*, at P1 to P6) was set to 9.5 [43]. The ECT forward problem was executed to obtain the ideal boundary capacitance measurement set for each of the six different positions.

Next, delamination in the form of a 1-mm-thick rectangular region of air (with a relative permittivity of 1) was incorporated in the center of the CFRP FE model. The size of the delamination was changed according to the five damage cases considered. The ECT forward problem was executed to calculate the capacitance responses for each damage case and at the six different positions in the sensing region. These capacitance datasets were compared with the undamaged results, and the squares of their RMS values were plotted in Fig. 13 as a function of damage case.

From these results, it was found that larger delamination resulted in a greater change in boundary capacitance response with respect to the baseline as indicated by the increase in RMS values. Linear least-squares regression lines were fitted to these RMS values corresponding to different damage sizes. The corresponding noise powers shown in Table 3 were also

Table 3. RMS values of measurement noise at different positions

Position	P1	P2	P3	P4	P5	P6
Noise power (F^2)	1.56E-32	1.46E-32	1.52E-32	1.57E-32	1.24E-32	1.56E-32
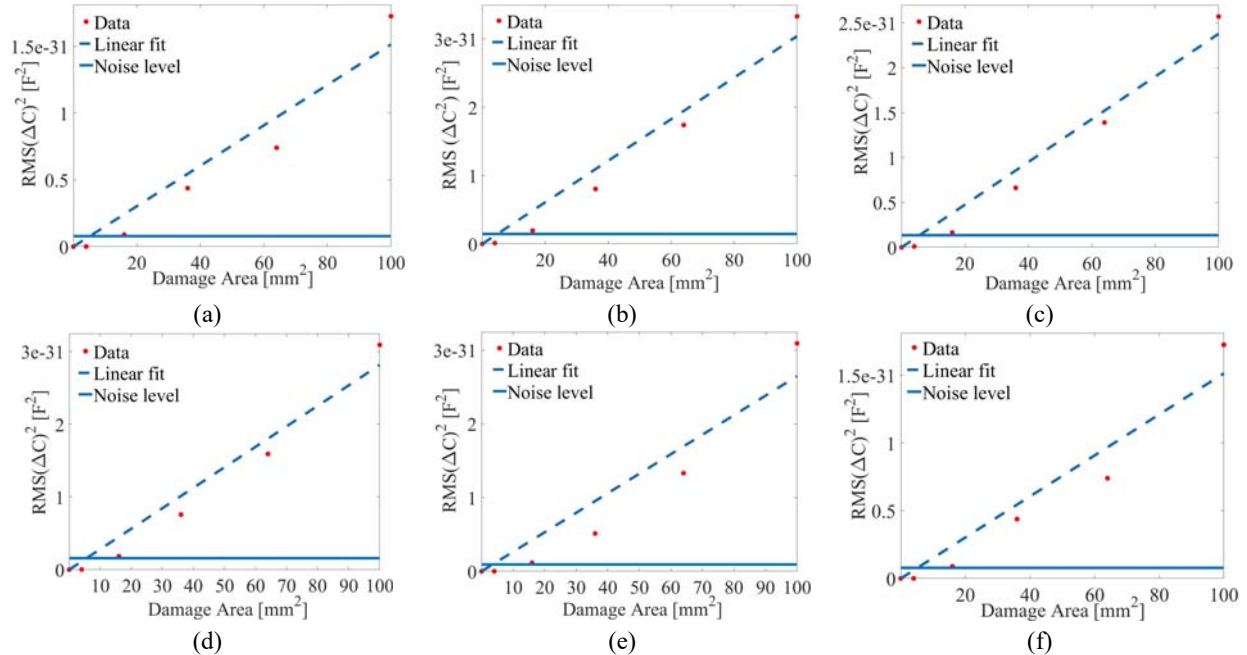
Figure 13. The measurement noise power and the square of the RMS values of the difference in estimated capacitance responses between damaged and undamaged specimens are plotted together for (a) P1, (b) P2, (c) P3, (d) P4, (e) P5, and (f) P6. Linear least-squares regression lines were overlaid.

plotted in Fig. 13. Here, the abscissa of the intersection of the noise level and the best-fit line is the effective resolution of the system. Since the delamination was square-shaped, the square roots of these values were evaluated to convert the estimated areas into equivalent linear lengths, and the results are reported in Table 4. Overall, the resolution of the planar ECT system was between 2.16 to 2.38 mm with respect to different positions in the sensing region. In principle, this resolution would forbid the system from detecting delamination of sizes similar to the D1 case (note that C-scan was also unable to confirm delamination). It should be noted that this resolution result is specific to this system and can be potentially improved by increasing the number of electrodes.

These resolution results can also be compared with other published studies, such as work done by McKenzie and Record [44]. A modified ECT hardware system was proposed, where a 4-mm-diameter conventional ECT electrode array was employed for monitoring sections of aircraft wings. The proposed system could locate the position of a wire-under-test inside a 4-mm-diameter casing with an accuracy of 0.1 mm. Despite this success, the system was based on conventional ECT (*i.e.*, circular ECT electrode array) that was tiny (~4 mm

in diameter). This test setup may not be suitable for inspecting large composite aircraft wings, and the accuracy of the system could also change with electrode array geometry.

Loyola *et al*. [45] also showed that the resolution of an EIT imaging system is equal to the inverse of the square root of the number of independent measurements. More independent measurements can be obtained for image reconstruction by increasing the number of interrogation electrodes in the planar ECT system. Doing so would improve resolution and enhancing detectability of subsurface features. In addition to investigating the use of more independent measurements on image quality, effects of electric field strength and frequency will also be characterized in subsequent future studies.

5. Conclusions

A noncontact planar ECT permittivity imaging method was investigated for characterizing and visualizing delamination in CFRP components. First, the planar ECT forward and inverse algorithms were developed, and a planar ECT electrode array was assembled in the laboratory. Tests were conducted to verify that the system was able to identify the locations,

Table 4. Resolution of the planar ECT system corresponding to different positions

Position	P1	P2	P3	P4	P5	P6
Resolution [mm]	2.25	2.217	2.38	2.36	2.16	2.29

shapes, and sizes of foreign objects (*i.e.*, 3D-printed PLA blocks) placed in the sensing region. Second, damage was introduced to PLA panels by introducing a thin rectangular void during 3D-printing. The ECT results showed that these artificial delamination features could be observed. Based on these results, experiments were performed to validate imaging of subsurface delamination in CFRP panels. CFRP panels with different sizes of single-layer delamination were fabricated by VARTM. ECT tests were conducted, and the results clearly showed the sizes and locations of damage. In addition, an average position error of ~ 6.35 mm and resolution of ~ 2.16 mm were found. The vision is that planar ECT can be used as a hand-held instrument for scanning large composite structural components for rapid nondestructive inspection. Future studies will focus on electrode array scale-up and testing the system on larger composite panels with more complex damage features.

Acknowledgments

References

1. Stark W, and Bohmeyer W. Non-destructive Evaluation (NDE) of Composites: Using Ultrasound to Monitor the Curing of Composites. Non-Destructive Evaluation (NDE) of Polymer Matrix Composites 2013; 136-181.
2. Hussain M, Nakahira A, and Niihara K. Mechanical Property Improvement of Carbon Fiber Reinforced Epoxy Composites by Al_2O_3 Filler Dispersion. Materials Letters. 1996; 26(3): 185-191.
3. Natali A, Manzi S, and Bignozzi MC. Novel Fiber-Reinforced Composite Materials Based on Sustainable Geopolymer Matrix. Procedia Engineering. 2011; 1124-1131.
4. Aoki Y, Suemasu H, and Ishikawa T. Damage Propagation in CFRP Laminates Subjected to Low Velocity Impact and Static Indentation. Advanced Composite Materials. 2007; 16(1): 45-61.
5. Ishai O, and Shragai A. Effect of Impact Loading on Damage and Residual Compressive Strength of CFRP Laminated Beams. Composite Structures. 1990; 14(4): 319-337.
6. Gholizadeh S. A Review of Non-Destructive Testing Methods of Composite Materials. Procedia Structural Integrity. 2016; 1 50-57.
7. Cantwell WJ, and Morton J. Detection of Impact Damage in CFRP Laminates. Composite Structures. 1985; 3(3-4): 241-257.
8. Bolduc M, and Roy C. Evaluation of Impact Damage in Composite Materials using Acoustic Emission. Composite Materials: Fatigue and Fracture. 1993; 4
9. Pappas YZ, and Kostopoulos V. Toughness Characterization and Acoustic Emission Monitoring of a 2D Carbon/Carboncomposite. Engineering Fracture Mechanics 2001; 68(14): 1557-1573.
10. Gustafson CG, and Selden RB. Monitoring Fatigue Damage in CFRP using Acoustic Emission and Radiographic Techniques. Delamination and Debonding of Materials. 1985;
11. Halmshaw R. Development of Industrial Radiography Technique over the Last 50 years. Insight. 1995; 37(9): 684-687.
12. Loyola BR, Saponara VL, Loh KJ, Briggs TM, O'Bryan G, and Skinner JL. Spatial Sensing using Electrical Impedance Tomography. IEEE Sensors. 2013; 13(6): 2357-2367.
13. Thomas AJ, Kim J, Tallman TN, and Bakis CE. Damage Detection in Self-Sensing Composite Tubes via Electrical Impedance Tomography. Composites Part B: Engineering. 2019; 177 107276.
14. Yang WQ, and Peng L. Image Reconstruction Algorithms for Electrical Capacitance Tomography. Measurement Science and Technology. 2002; 14(1): R1-R13.
15. Soleimani M. Image and Shape Reconstruction Methods in Magnetic Induction Tomography and Electrical Impedance Tomography. Ph.D. . School of Mathematics. University of Manchester. Manchester, England. 2005.
16. Dyakowski T, York T, Mikos M, Vlaev D, Mann R, Follows G, Boxman A, and Wilson M. Imaging Nylon Polymerisation Processes by Applying Electrical Tomography. Chemical Engineering Journal,. 2000; 77(1-2): 105-109.
17. Gut Z, and Wolanski P. Flame Imaging Using 3D Electrical Capacitance Tomography. Combustion Science and Technology. 2010; 182(11-12): 1580-1585.
18. Soleimani M, and Lionheart WR. Nonlinear Image Reconstruction for Electrical Capacitance Tomography using Experimental Data. Measurement Science and Technology. 2005; 16(10): 1987-1996.
19. Wang H, Liu S, Jiang F, and Yang W. 3D Presentation of Images with Capacitance Tomography, Conf Proc 3rd World Congress on Industrial Process Tomography. 2003; 331-336.
20. Zhang W, Wang C, Yang W, and Wang C-H. Application of Electrical Capacitance Tomography in Particulate Process Measurement–A Review. Advanced Powder Technology. 2014; 25(1): 174-188.
21. Gupta S, and Loh KJ. Numerical Simulations of Railroad Track Damage Characterization using Non-Contact Tomography, Conf Proc First International Workshop on Structural Health Monitoring for Railway Systems. 2016.
22. Gupta S, and Loh KJ. Characterization and Localization of Sub-Surface Structural Features using Non-Contact Tomography, Conf Proc ASME Smart Materials, Adaptive Structures, and Intelligent Systems (SMASIS) Conference. 2016.
23. Yin X, and Hutchins DA. Non-Destructive Evaluation of Composite Materials Using a Capacitive Imaging Technique. Composites Part B: Engineering. 2012; 43(3): 1282-1292.
24. Zhang Y, Zhao L, Wen Y, and Sun D. Non-destructive Evaluation of Adhesive Layer Using a Planar Array Capacitive Imaging Technology, Conf Proc SPIE Smart Structures and Materials+ Nondestructive Evaluation and Health Monitoring. 2016; 98042D-98042D-7.
25. Gupta S, Fan G, and Loh KJ. Noninvasive Monitoring of Epoxy Curing. IEEE Sensors Letters. 2017; 1(5): 1-4.
26. Fan G, Gupta S, and Loh KJ. Curing and Subsurface Damage Monitoring of Epoxy-based Composites. Structural Health Monitoring. 2018; 18(4): 1040-1055.
27. Gupta S, and Loh KJ. Noncontact Electrical Permittivity Mapping and pH-Sensitive Thin Films for Osseointegrated Prosthesis and Infection Monitoring. IEEE Transactions on Medical Imaging. 2017; 36(11): 2193-2203.
28. Gupta S, Lee H-J, Loh KJ, Todd MD, Reed J, and Barnett AD. Noncontact Strain Monitoring of Osseointegrated Prostheses. Sensors. 2018; 18(9): 3015.

29.   Ye Z, Banasiak R, and Soleimani M. Planar Array 3D Electrical Capacitance Tomography. Insight-Non-Destructive Testing and Condition Monitoring. 2013; 55(12): 675-680.
30.   Wang F, Marashdeh Q, Fan LS, and Warsito W. Electrical Capacitance Volume Tomography: Design and Applications. Sensors. 2010; 10(3): 1890-1917.
31.   Hu X, and Yang W. Planar Capacitive Sensors – Designs and Applications. Sensor Review. 2010; 30(1): 14-39.
32.   Chen D, Hu X, and Yang W. Design of a Security Screening System with a Capacitance Sensor Matrix Operating in Single-Electrode Mode. Measurement Science and Technology. 2011; 22(11): 114026.
33.   Diamond GG, Hutchins DA, Gan TH, Purnell P, and Leong KK. Single-Sided Capacitive Imaging for NDT. Insight-Non-Destructive Testing and Condition Monitoring. 2006; 48(12): 724-730.
34.   Ye Z, Banasiak R, and Soleimani M. Planar Array 3D Electrical Capacitance Tomography. Insight-Non-Destructive Testing and Condition Monitoring. 2013; 55(12): 675-680.
35.   Tholin-Chittenden C, Abascal JF, and Soleimani M. Automatic Parameter Selection of Image Reconstruction Algorithms for Planar Array Capacitive Imaging. IEEE Sensors Journal. 2018; 18(15): 6263-6272.
36.   Li Y, and Soleimani M. Imaging Conductive Materials with High Frequency Electrical Capacitance Tomography. Measurement. 2013; 46
37.   Hosani EA, Zhang M, Abascal JFPJ, and Soleimani M. Imaging Metallic Samples using Electrical Capacitance Tomography: Forward Modelling and Reconstruction Algorithms. Measurement Science and Technology. 2016; 27 115402.
38.   Fang W. A Nonlinear Image Reconstruction Algorithm for Electrical Capacitance Tomography. Measurement Science and Technology. 2004; 15 2124-2132.
39.   Soleimani M. Three-Dimensional Electrical Capacitance Tomography Imaging. Insight. 2006; 48(10): 613-617.
40.   Vauhkonen M. Electric Resistance Tomography and Prior Information. Ph.D. Natural and Environmental Sciences. University of Kuopio. Kuopio, Finland. 1997.
41.   Yorkey J, Webster JG, and Tompkins WJ. Comparing Reconstruction Algorithms for Electrical Impedance Tomography. IEEE Transactions on Biomedical Engineering. 1987; 34(11): 843-852.
42.   Adler A, Arnold JH, Bayford R, Borsic A, Brown B, Dixon P, Faes TJ, Frerichs I, Gagnon H, Gärber Y, and Grychtol B. GREIT: A Unified Approach to 2D Linear EIT Reconstruction of Lung Images. Physiological Measurement. 2009; 30(6): S35–S55.
43.   Elimat ZM, Hamideen MS, Schulte KI, Wittich H, Vega ADl, Wichmann M, and Buschhorn S. Dielectric Properties of Epoxy/Short Carbon Fiber Composites. Journal of Materials Science. 2010; 45(19): 5196-5203.
44.   McKenzie G, and Record P. Prognostic Monitoring of Aircraft Wiring using Electrical Capacitive Tomography. Review of Scientific Instruments. 2011; 82(12): 124705.
45.   Loyola BR, Briggs TM, Arronche L, Loh KJ, Saponara VL, O'Bryan G, and Skinner JL. Detection of Spatially Distributed Damage in Fiber-Reinforced Polymer Composites. Structural Health Monitoring. 2013; 12(3): 225-239.